**Article:**
Zhang, H, Wang, D, Han, Y et al. (3 more authors) (2018) High photoactivity rutile-type TiO2 particles co-doped with multiple elements under visible light irradiation. Materials Research Express, 5 (10). ARTN 105015. pp. 1-12. ISSN 2053-1591

https://doi.org/10.1088/2053-1591/aad9d7

# High photoactivity rutile-type $TiO_2$ particles co-doped with multiple elements undervisible light irradiation

Hui Zhang[1], Dou Wang[1], Ye Han[1], Qi Tang[1], Hailiang Wu[1] and Ningtao Mao[2]

[1] School of Textile Science and Engineering, Xi'an Polytechnic University, Xi'an 710048, People's Republic of China
[2] School of Design, University of Leeds, Leeds, LS2 9JT, United Kingdom

E-mail: hzhangw532@xpu.edu.cn

Keywords: hydrothermal synthesis, multi-elements doping, photoactivity

Abstract

In this study, wool fibers were used as the source of doping species to prepare the rutile-type $TiO_2$ photocatalyst for the treatment of dyeing wastewaters based on the hydrothermal method. The urchin-like rutile-type $TiO_2$ particles were characterized by scanning electron microscopy, energy-dispersive x-ray, laser particle size analyzer, x-ray powder diffraction, transmission electron microscopy, Brunauer–Emmett–Teller nitrogen adsorption-desorption, x-ray photoelectron spectroscopy, thermal gravimetric analysis, diffuse reflectance spectroscopy and photoluminescence spectra techniques. The photocatalytic degradation of rhodamine B dye aqueous solution was measured under visible light irradiation. The experimental results show that the urchin-like rutile type $TiO_2$ particles produced by using wools exhibit much higher photocatalytic activity than those urchin-like rutile-type $TiO_2$ particles without using wools under visible light irradiation. The high photoactivity of the urchin-like rutile-type $TiO_2$ particle is attributed to the co-doping of multiple elements including carbon, oxygen, nitrogen, sulfur and chlorine, the larger specific surface area, and the positive zeta potential. This research provides a simple route to synthesize efficient $TiO_2$ photocatalyst with high photocatalytic activity.

## 1. Introduction

It is reported that the photocatalytic activity of anatase-type or anatase/rutile coupled titanium dioxide ($TiO_2$) is generally higher than that of rutile-type $TiO_2$ for the photocatalytic oxidation of organic compounds like 2-propanol [1] and phenol [2]. The difference in photoactivity between rutile and anatase $TiO_2$ is mainly due to the intrinsic recombination of photogenerated electron and hole pairs [3]. The mechanism has been well explained by the use of first principle density functional theory [4]. Even so, rutile-type $TiO_2$ has been applied to the photocatalytic degradation of hazardous contaminants exposure to ultraviolet (UV) irradiation because of its unique features, such as high refractive index, non-toxicity and chemical stability [5]. It is found that the photo-oxidative ability of rutile $TiO_2$ can surpass the anatase $TiO_2$ for the decomposition of4-chlorophenol [6]. The mesoporous rutile $TiO_2$ has a good photoactivity for gas-phase photo-oxidation of a mixture of benzene and methanol [7]. The surface defects of rutile $TiO_2$ can promote the separation of electron-hole pairs under UV irradiation [8]. The micro-cavities on rutile $TiO_2$ could act as micro-capacitors for electronic storage, which results in the efficient separation of photogenerated electron-hole pairs [9]. As the Ti–Ti distance on rutile is smaller than that on anatase, the Ti–OO–Ti structure can be formed on rutile $TiO_2$ surface, thus leading to $O_2$ [10].

It has been demonstrated that the photoactivity of rutile-type $TiO_2$ is primarily dominated by the specific surface area [11], morphology [12], band-gap energy [13], crystallinity [14], porosity [15], crystal facets [16], structure evolution [17], crystalline size [18], crystal splitting [19] and so on. It can also be enhanced by the coupling of equal amounts of the reduced and oxidized rutile $TiO_2$ powders [20]. The {1101 crystal facets have a great potential to improve the photoactivity of rutile $TiO_2$ [21]. The exposed {0011 [22] or {1111 [23] crystal facets can induce the separation of electrons and holes. The {1111 crystal facets have higher photocatalytic activity than {1101 facets due to the surface unsaturated $_{O2c}$ modes on the {1111 facets [24]. In addition, the photoactivity of rutile $TiO_2$ is influenced by its aspect ratios because of the different separation efficiencies of photogenerated carriers on different facets [25].

Many strategies including metal ions, metal oxides, and non-metal elements doping have been applied to modify rutile-type $TiO_2$ to extend the visible light absorption [26]. Regarding the non-metal doped rutile $TiO_2$, the chemical elements of [27], $C^{4+}$ and $S^{4+}$ [28] and halogen element [29] have been used to inhibit the recombination of electron-hole pairs in $TiO_2$ by capturing the photo-induced electrons via various synthesis routes. The strong visible-light absorption

can also be realized through coordination with peroxide to improve the photocatalytic performance of rutile $TiO_2$ [30]. Furthermore, the rutile $TiO_2$ doped with upconversion luminescence agent (40 $CdF_2$·60 $BaF_2$·1.0 $Er_2O_3$) [31], N, B and Pt [32], N, O, Pt, V and Sb [33], BiOCl [34], Ag and fluorination [35], Sm and C [36] have been prepared.

More recently, much attention has been paid to the development of rutile-type TiO2 doped with multi-elements [37]. For instance, the photogenerated charge separation can be promoted by modification of rutile TiO2 with chlorine and phosphate coupled with carbon nanotubes to improve the photocatalytic conversion of CO2 to CH4 and CO [38]. Carbon, nitrogen, and sulfur co-doped rutile TiO2 nanorods have been synthesized by two-step hydrothermal method. They have much higher visible-light-driven photocatalytic activity in degrading rhodamine B dye [39]. The dopant elements of Mo, Fe, and N can decrease the band gap energy of rutile TiO2 [40]. The rutile TiO2 nanowires co-implanted with carbon and nitrogen atoms exhibit the improved visible light photocatalytic activity because of the enhanced visible light absorption capability and the efficient separation and transfer of photogenerated carriers [41]. It is known that keratin wool is composed of 20 common α-amino acids, which consist of around 50 wt% carbon, 7 wt% hydrogen, 22 wt% oxygen, 16 wt% nitrogen and 5 wt% sulfur [42]. The hydrolysis of keratin wool occurs by the cleavage of peptide bonds under acid hydrothermal conditions [43]. Herein, the wool fiber is used as the doping source to improve the visible-light photocatalytic activity of rutile-type TiO2. The urchin-like rutile-type TiO2 particles co-doped with carbon, oxygen, nitrogen, sulfur, and chlorine have been successfully fabricated by a facile one-step hydrothermal process by using titanium tetrachloride and wools to exploit the potential application in wastewater treatments.

## 2. Experimental section

### 2.1. Materials

Wool fibers were friendly provided by a local wool textile mill. The chemical reagents were of analytical grade, including titanium tetrachloride ($TiCl_4$, CAS: 7550-45-0), sodium carbonate ($Na_2CO_3$), absolute ethanol ($CH_3CH_2OH$), acetone ($CH_3COCH_3$), and rhodamine B (RB, $C_{28}H_{31}ClN_2O_3$, CAS: 81-88-9). Deionized water was used to prepare the solution during the experiment.

### 2.2. Hydrothermal synthesis of rutile-type $TiO_2$ particles

About 1.0 g of as-obtained wool fibers was firstly soaked in 50 ml of 1.0 g $L^{-1}$ sodium carbonate aqueous solution at 60 °C for 2 h according to the material to liquor ratio of 1:50. The wool fibers were then washed twice with deionized water, acetone and anhydrous ethanol solutions at ambient temperature for 10 min, respectively. The cleaned wool fibers were finally dried in an oven at 60 °C for 24 h.

Rutile-type titanium dioxide ($TiO_2$) particles were prepared by using a modified hydrothermal method as reported previously [44]. 5 ml of titanium tetrachloride was added drop-wise in5 ml of anhydrous ethanol solution under vigorous stirring at 20 °C. The mixture was then diluted with 70 ml of deionized water under stirring. An optimal amount of cleaned wool fibers (0.4 g) was immersed in the above suspension. The suspension along with the fibers was immediately transferred to a 100 ml PTFE tank, which was sealed in a stainless steel autoclave. The autoclave was put in a reactor and heated to 120 °C at a heating rate of 1.5 °C/min. After 3 h, the PTFE tank cooled down to room temperature. The white mixture solution was centrifuged at 12 000 revolutions per minute for 10 min using a TG16-WS high-speed centrifuge (Hunan Xiang Yi Laboratory Instrument Development Co., Ltd, China). The precipitated particles were sonically washed twice for 15 min in acetone, anhydrous ethanol and deionized water at 40 kHz and 100 W respectively, and finally dried in an oven at 120 °C. The as-synthesized particles were denoted as IV + W. For comparison, the control rutile-type $TiO_2$ particles (denoted as IV) were also prepared by the same above method without adding of wool fibers. All finally as-synthesized particles were finely ground with an agate mortar prior to usage.

### 2.3. Characterization methods

The surface morphologies of as-synthesized particles were observed on a Zeiss Evo18 Merlin compact scanning electron microscopy (SEM, Carl Zeiss AG, German) at 10 kV.

The element compositions of as-synthesized particles were analyzed by an Oxford Inca energy dispersive x-ray (EDX) spectroscopy attached to the above SEM.

The particle size distributions and zeta potentials of as-synthesized particles were evaluated using a Malvern Zetasizer Nano ZS90 analyzer (Model ZEN3690, Malvern Instruments, UK).

The crystal structures of as-synthesized particles were identified on an XRD-7000S x-ray diffractometer (Shimadzu Corp., Japan) operating at 40 kV and 40 mA using Cu $K\alpha_1$ radiation from 10° to 80° at a scanning speed of 8 deg $min^{-1}$.

The crystallite sizes (D) of $TiO_2$ particles were calculated by Scherrer equation (1) [45]:

$$D = K\lambda/\beta cos\theta \quad (1)$$

where K was the shape factor (0.89); $\lambda$ was the wavelength of Cu $K\alpha_1$ radiation (0.154 0562 nm); $\beta$ was the full width at half maximum (FWHM) of the diffraction peak, and $\theta$ was the Bragg angle of the diffraction peak. The microstructures of as-synthesized particles were examined by a JEOL3010 transmission electron microscopy (TEM, JEOL Ltd, Japan) operating at 200 kV. A small amount of $TiO_2$ particles was sonicated for 10 min in ethanol solution, and a drop of the suspension was then deposited onto a carbon-coated copper grid for TEM imaging.

The nitrogen adsorption-desorption isotherms of as-synthesized particles were performed on a Gemini VII 2390 surface area analyzer (Micromeritics Instrument Corp., USA) at 77K. Prior to measurement, the sample was out-gassed under vacuum for 24 hat 120°C. Brunauer–Emmett–Teller (BET) model was applied to adsorption isotherm branch in the relative pressure range ($P/P_0$) below 0.25 to calculate surface area.

The chemical bonding states of as-synthesized particles were characterized by an Axis Ultra x-ray photoelectron spectroscopy (XPS, Kratos Analytical Ltd, UK) using monochromatic Al Ka (1486.7eV) line at a power of 100 W (10mA, 10kV) with the vacuum about $10^{-8}$ Torr. The binding energies were calibrated to the $C_{1s}$ peak at 284.8eV of the surface adventitious carbon to compensate the shift caused by charge effect.

The thermal stabilities of as-synthesized particles were measured on a TGA Q500 thermogravimetric analyzer (TGA, TA Instruments) from 40°C to 600°C at a nitrogen flow rate of40 ml $min^{-1}$ and a heating rate of10 °C $min^{-1}$.

The diffuse reflectance spectra (DRS) of as-synthesized particles were conducted on a Lambda 950 UV-Visible spectrophotometer (PerkinElmer Inc., USA) equipped with a diffuse reflectance accessory over the wavelength range of 200–800 nm at a scanning rate of 600 nm $min^{-1}$.

The photoluminescence (PL) spectroscopies of as-synthesized particles were investigated on a PerkinElmer LS-55 fluorescence spectrophotometer using a Xenon discharge lamp with an excitation wavelength of 320nm at a scanning rate of 1000 nm $min^{-1}$.

### 2.4. Photocatalytic activity test

The photocatalytic degradation of the model pollutant of RB dye aqueous solution by rutile-type $TiO_2$ particles was carried out on an YM-GHX-V photochemical reactor (Shanghai Yuming Instrument Co. Ltd, China) equipped with a 1000 W xenon lamp. 0.03 g of as-synthesized particles was added in 50 ml of 5 mg $L^{-1}$ RB dye aqueous solution. The mixture was sonicated for 30 min at 40 kHz and 100 Wand then put in a dark place to reach the adsorption-desorption equilibrium. After 1.5 h, the mixture solution was transferred to a quartz tube, which was irradiated with visible light irradiation under magnetic stirring. The UV cut-off filter was used to block off UV rays. The intensity of visible light was measured to be 10690 Lux by a TES 1332A light meter (TES Electrical Electronic Co. Ltd, Taiwan). About 5 ml of the mixture solution was centrifuged for 10 min at a speed of 12 000 rpm using the TG16-WS high-speed centrifuge at certain time intervals. The supernatant was extracted from the solution and the absorbance curve of RB dye solution was recorded using a UV-1601 spectrophotometer (Beijing Rayleigh Analytical Instrument Co. Ltd, China).

## 3. Results and discussion

### 3.1. Morphology observation, element composition, and particle size

The SEM images, EDX spectra and particle size distributions of as-synthesized particles are illustrated in Figure 1. The high-magnification SEM images of both particles clearly indicate that the as-synthesized particles are composed of spherical particles roughly 100 nm in diameters, which are liable to agglomerate together to form submicron-sized clusters due to their high surface energy. There is no significant difference between the IV and IV + W particles. EDX spectra show that the IV particle is primarily made up of oxygen and titanium elements, suggesting the synthesis of $TiO_2$. Moreover, small amounts of carbon and chlorine elements are found. The carbon element may be caused by the ethanol and the chlorine element is induced by the residue of titanium tetrachloride. For the IV + W particle, besides the elements of carbon, oxygen, chlorine, and titanium, a trace amount of sulfur element is detected, which is attributed to found in the IV + W particle. This might be because the amount of nitrogen element is beyond the detection limit of the EDX detector. The particle size distributions are in accord with the SEM images. The IV and IV + W particles have almost the same particle size distributions in the range of 250–1500 nm.

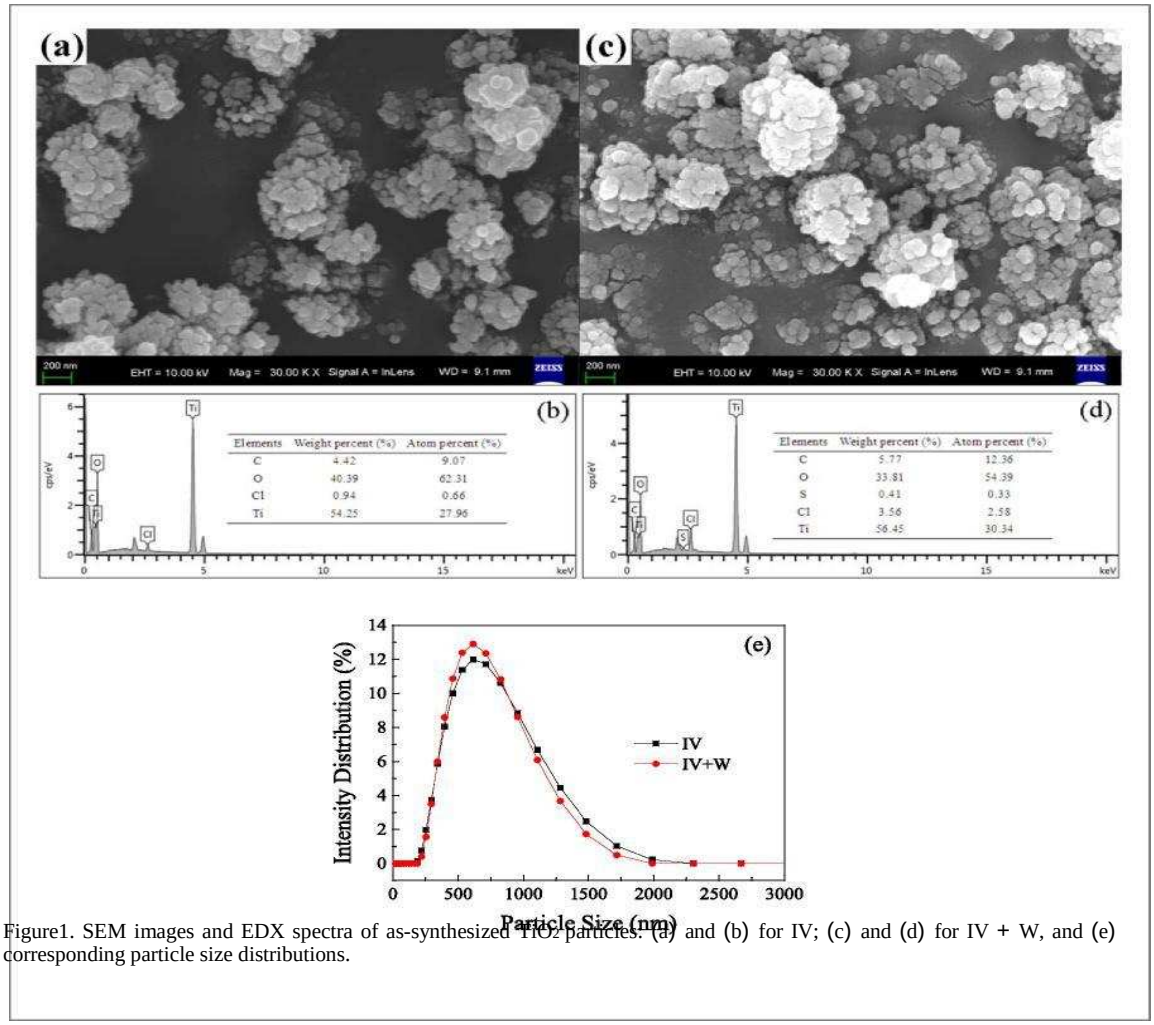


Figure1. SEM images and EDX spectra of as-synthesized $TiO_2$ particles: (a) and (b) for IV; (c) and (d) for IV + W, and (e) corresponding particle size distributions.

To further investigate the microscopic structures of as-synthesized particles, the TEM technique is used and the TEM and high-resolution TEM (HRTEM) images and selected area electron diffraction (SAED) patterns are represented in figure 2. The TEM micrographs for both IV and IV + W $TiO_2$ particles confirm that these sphere particles shown in SEM are actually urchin-like particles, which are made up of rod-like nano-scaled particles of mean diameter around 15 nm. It has been verified that the morphology of rutile $TiO_2$ can be controlled by changing the molar ratios of titanium tetrachloride, ethanol, and water, resulting in different superstructures like nanorod, nanoflower and urchinlike superstructures [44]. The three-dimensional urchin-like structure can enhance the light harvesting and the transfer of reactant molecules from bulk solution to the reactive sites on $TiO_2$ [46]. In more detail, the HRTEM analysis found that the surface of IV nano-crystals is very clean. On the contrary, a layer of organic compound is coated on the surface of IV + W nano-crystals, implying the doping of wool keratin with urchin-like $TiO_2$ particles. The inter-planar distances are measured to be 0.335 nm for the IV specimen and 0.332 nm for the IV + W specimen respectively, which are slightly larger than the typical value (0.325 nm) of the (110) plane of rutile-type $TiO_2$ [25]. This is due to the fact that the substituted Gland S (see XPS section) cause the lattice distortion of $TiO_2$ because of their electronegativity and larger atomic radii than those of O, thus resulting in some defects in the $TiO_2$ [47]. The exposed (110) crystal plane facilitates the separation of electrons and holes [48] and the selective adsorption of RB dye [49]. As can be seen from SAED patterns, the diffraction rings of the IV and IV + W particles reveal that the as-synthesized urchin-like particles are crystalline. These diffraction rings can be well indexed to (110), (101), (111), (211), (301), and (202) crystal planes of rutile $TiO_2$ [50].

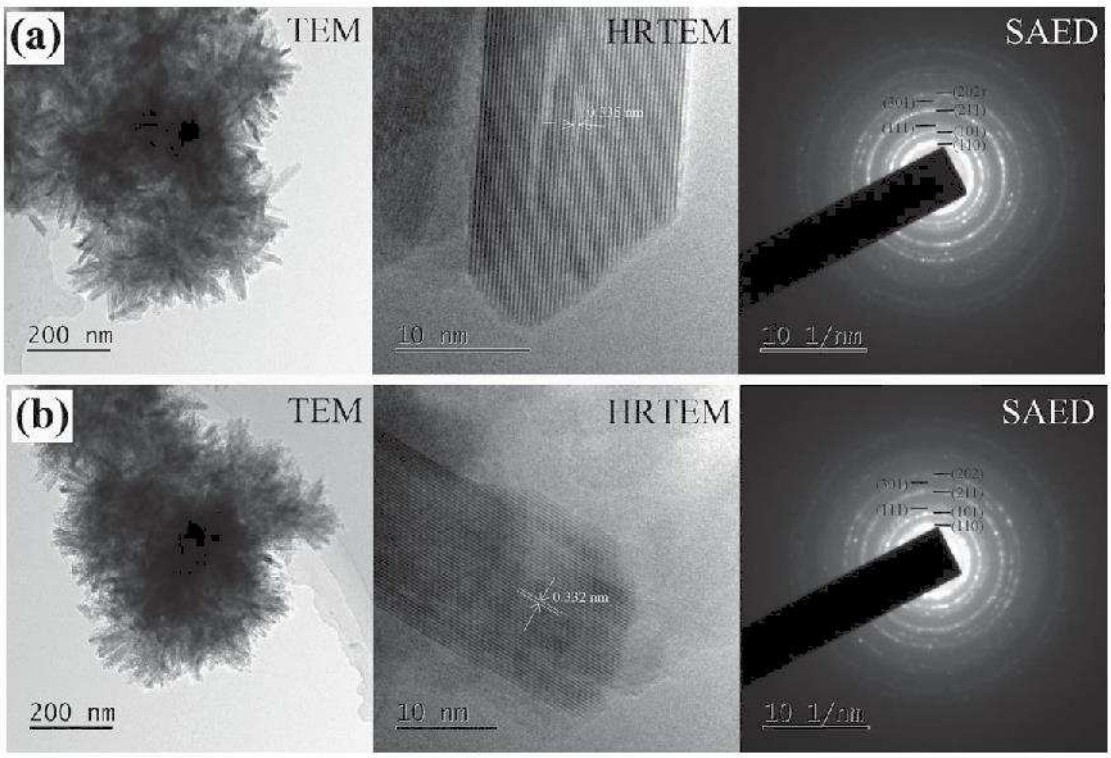


Figure 2. TEM and high resolution TEM (HRTEM) images, and selected area electron diffraction (SAED) patterns of (a) IV and (b) IV + WTiO2 particles.

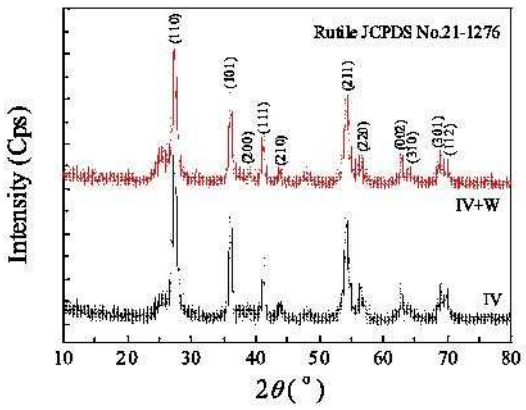


Figure 3. XRD patterns of as-synthesized

### 3.2. Crystal structure analysis

The x-ray diffraction (XRD) patterns of as-synthesized particles are presented in figure 3. The diffraction patterns for both of particles look very similar to each other. They exhibit the intensified peaks at 27.4°, 36.1°, 41.2°, 54.4°, 56.5°, 62.8°, 69.0° and 69.8°, corresponding to (110), (101), (111), (211), (220), (002), (301) and (112) crystal planes of rutile-type $TiO_2$ (JCPDS Card no. 21-1276) [39], respectively. This means that the IV and IV + W $TiO_2$ particles consist of single-phase rutile structure. It has been confirmed that the (002) orientation growth can be enhanced while the (101) orientation growth can be restrained by using the ethanol under hydrothermal conditions, thus reducing the size of the rutile $TiO_2$ [51]. The average crystallite sizes of as-synthesized $TiO_2$ are calculated to be 16.4 nm for IV particle and 12.9 nm for IV + W particle on the basis of the x-ray line broadening at (110), (101), (111) and (211) planes using Scherrer's equation, respectively. It indicates that the keratin macromolecules resulting from wools can control the growth of $TiO_2$ nanocrystals during hydrothermal processing to a certain extent [52].

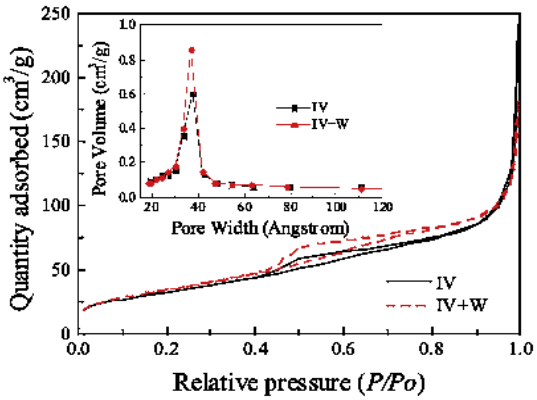


Figure 4. N2 adsorption-desorption isotherms and corresponding pore-size distribution profile (inset) of as-synthesized TiO2 particles.

### 3.3. Pore structure analysis

The nitrogen adsorption-desorption isotherms inserted with pore-size distribution profiles of as-synthesized particles are depicted in figure 4. The adsorption-desorption isotherms for both particles measured volumetrically at 77 K are identified as type II isotherm according to the International Union of Pure and Applied Chemistry (IUPAC) classification, which is characteristic of nonporous or macroporous materials [44]. This is strongly supported by the HRTEM images of rutile-type $TiO_2$ urchin-like particles. As the relative pressure increases, the quantity absorbed gradually increases from 0.1 to 0.9 relative pressures. Beyond 0.9 $P/P_0$, there is an enhanced uptake of nitrogen. It implies that the monolayer and multilayer formation occur in the IV and IV + W $TiO_2$ particles. At the same time, the small hysteresis loops having the forced closure points appearing at about $P/P_0 = 0.4$ are associated with the filling of macropores produced by inter-aggregated secondary urchin-like superstructure [44] and the physical nature of adsorbate nitrogen gas [53]. The BET specific surface area of the IV + W particle is calculated to be 124.15 $m^2\ g^{-1}$, which is slightly larger than 117.84 $_{m2}\ g{-1}$ of the IV one. The higher surface area facilitates the multiple light reflection and beneficial electron conduction [54]. Additionally, based on the Barrett–Joyner–Halenda (BJH) method, the adsorption cumulative volumes of pores between 1.7 and 300 nm width are calculated as 0.3622 and 0.2682 $cm_3\ g^{-1}$ for the IV and IV + W particles, respectively. However, the sharp peaks at around 4 nm pore width in the pore-size distribution profiles, which is related to the closure point of the hysteresis loop, cannot reflect the real 4 nm mesopores [55].

### 3.4. Surface chemical bonding analysis

The survey spectra and core level spectra of$C_{1s}$, $O_{1s}$, $N_{1s}$, $Cl_{2p,\ and\ Ti2p}$ for the as-synthesized $TiO_2$ particles are displayed in figure5. The results of XPS elemental analysis are listed in table 1. In comparison with the IV particle, besides the elements of C, O, Ti and Cl, the N element is identified, but the S element is not detected in the IV + W particle. Combined with the EDX and TEM analyses, it is concluded that the S element derived from wool keratin is completely doped into the bulk phase $TiO_2$.

In the case $_{ofC1s}$ XPS spectra, when wool fibers are added to the titanium tetrachloride mixture solution, the subpeaks at 282.86,284.81,286.42 and 288.65 eV, corresponding to the binding energies of C–$Ti^{4+}$/$Ti^{3+}$, C–C/ C–H, C–O and C=O [39], are shifted to 283.04,284.79,286.48 and 288.79 eV respectively. The binding energy of C–$Ti^{4+}$/$Ti^{3+}$ in the IV particle is due to the ethanol, while it is enhanced by the hydrolysis of wools in the IV + W particle.

In addition, a new subpeak at 285.38 eV (C–N) is observed only in the IV + W particle. The corresponding $N_{1s}$ XPS spectra can be separated into two subpeaks at 399.63 eV (N–$Ti^{4+}$/$Ti^{3+}$) and 400.15 eV (N–C/N–H). It is reported that nitrogen atoms can replace the surface saturated $_{O3c}$ on the {110} facets of rutile $TiO_2$ and act as unsaturated $_{N3c,}$ which can influence the adsorbent selectivity of RB [56].

The surface oxygen atoms on $TiO_2$ crystals depend on the surface orientation of the crystals, affecting the photocatalytic activity of $TiO_2$ [57]. The $_{O1s}$ peak of the IV particle can be deconvoluted into five subpeaks at 527.46 eV (O–$Ti^{3+}$), 529.85 eV (O–$Ti^{4+}$), 531.79 eV (O=C), 532.68 eV (O–C) and 533.63 eV (chemisorbed– OH bound to surface defects on $TiO_2$) [8]. They are shifted to 527.77, 529.95, 531.74, 532.15 and 533.58 eV respectively for the IV + W particle. Obviously, the binding energy of O–$Ti^{3+}$ for the IV + W particle strengthens to some degree compared with that of the IV particle, which is mainly ascribed to the hydrolysis of wools.

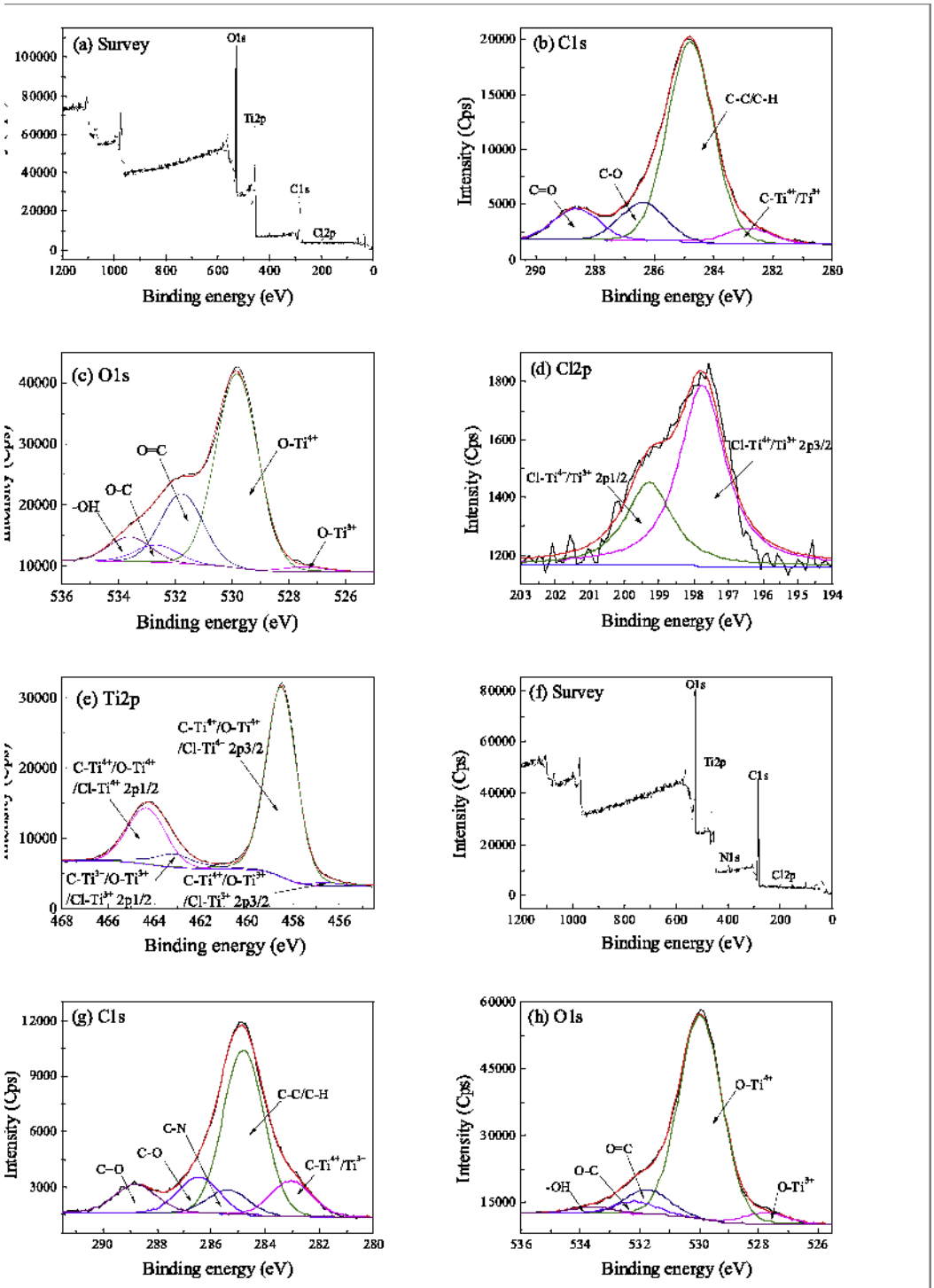


Figure 5. XPS survey and high resolution XPS spectra of as-synthesized $TiO_2$ particles: (a) survey spectra, (b) $_{C1s}$, (c) $_{O1s}$, (d) $_{Cl2p}$, and (e) $_{Ti2p}$ spectra for IV; (f) survey spectra, (g) $_{C1s}$, (h) $_{O1s}$, (i) $_{N1s}$, (j) $_{Cl2p}$, and (k) $_{Ti2p}$ spectra for IV + W.

Regarding the $_{Cl2p}$ spectra, the subpeaks at 199.76 eV (Cl–$Ti^{4+}$/$Ti^{3+}$ $_{2p3/2)}$ and 199.29 eV (Cl–$Ti^{4+}$/$Ti^{3+}$ $2p_{1/2}$) for the IV particle are ascribed to the substitutional $Cl^{-1}$ derived from titanium tetrachloride [46]. They are shifted to 198.38 and 200.62 eV after being added with the wool fibers respectively. Hence, some Cl ions are probably incorporated into $TiO_2$ crystal lattice by substitution of O atoms. The others exist in the form of interstitial $Cl^{-1}$ in the crystal cell [46].
The $Ti_{2p}$ XPS spectra for both particles are in line with the XPS spectra of$C_{1s}$, $O_{1s}$, $N_{1s}$, $^{and}$ $_{Cl2p.}$ The subpeaks at 464.34 and 458.51 eV (with a peak separation of 5.83 eV) in the IV particle are comparable to the binding energies of C–$Ti^{4+}$/O–$T^{4+}$/Cl–$Ti^{4+}_{2p1/2}$ respectively [58]. Meanwhile the subpeaks at 463.17 and 456.57 eV are assigned to C–$Ti^{3+}$/O–$T^{3+}$/Cl–$Ti^{3+}_{2p1/2}$ and C–$Ti^{3+}$/O–$Ti^{3+}$/Cl–$Ti^{3+}_{2p3/2}$. The $Ti^{3+}$ and $Ti^{4+}$ configuration can reverse the population disparity between holes and electrons reaching the surface of rutile $TiO_2$ [59]. For the IV + W particle, besides the C and O elements, the N element is doped with $TiO_2$.

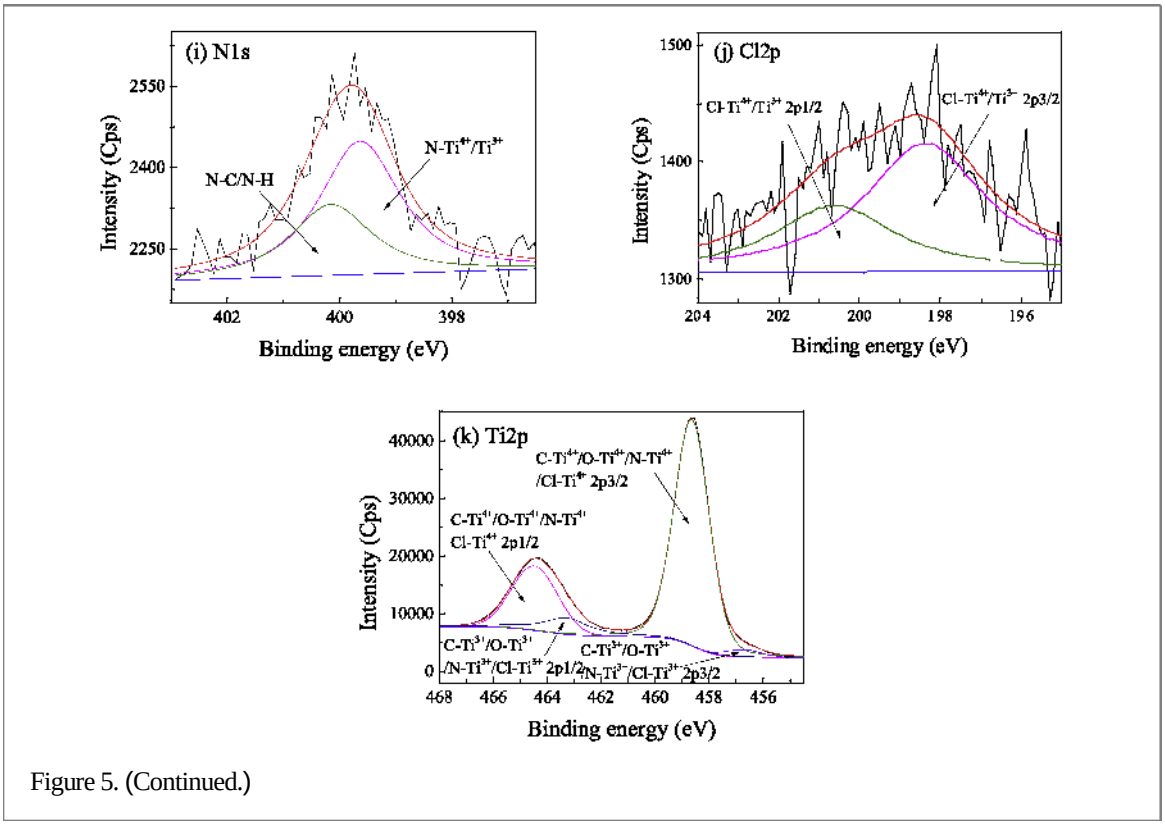


Figure 5. (Continued.)

Table1. The results of XPS elemental analysis of as-synthesized TiO2 particles.

| TiO2 | Name | Peak BE (eV) | FWHM (eV) | Atom percentage (%) |
|---|---|---|---|---|
| IV | C1s | 284.78 | 1.832 | 54.83 |
| | O1s | 529.76 | 1.637 | 34.40 |
| | Ti2p | 466.28 | 2.351 | 10.13 |
| | Cl2p | 201.45 | 1.660 | 0.64 |
| IV + W | C1s | 284.82 | 1.548 | 36.60 |
| | O1s | 529.56 | 1.505 | 45.01 |
| | Ti2p | 466.22 | 2.379 | 17.59 |
| | N1s | 401.60 | 1.947 | 0.57 |
| | Cl2p | 202.41 | 2.438 | 0.23 |

The subpeaks at 464.48 and 458.64 eV (with a peak splitting of 5.84 eV) are associated with C–$Ti^{4+}$/O–$Ti^{4+}$/N–$Ti^{4+}$/Cl–$Ti^{4+}_{2p1/2}$ and C–$Ti^{4+}$/O–$Ti^{4+}$/N–$Ti^{4+}$/Cl–$Ti^{4+}_{2p3/2}$ respectively, and the subpeaks at 463.30 and 456.74 eV are assigned to C–$Ti^{3+}$/O–$Ti^{3+}$/N–$Ti^{3+}$/Cl–$Ti^{3+}_{2p1/2}$ and C–$Ti^{3+}$/O–$Ti^{3+}$/N–$Ti^{3+}$/Cl–$Ti^{3+}_{2p1/2}$ respectively. The $Ti^{3+}$ related photo-absorption and visible light photocatalytic activity in $TiO_2$ arise from the Jahn–Teller induced splitting of the 3d orbitals of $Ti^{3+}$ ions via 3d → 3d transitions from the gap state to this empty resonant state [60].

Therefore, the XPS results show that both particles have the photocatalytic activities. The photoactivity of the IV + W particle is much higher than that of the IV one because of the co-doping of C, O, N, S, and Cl.

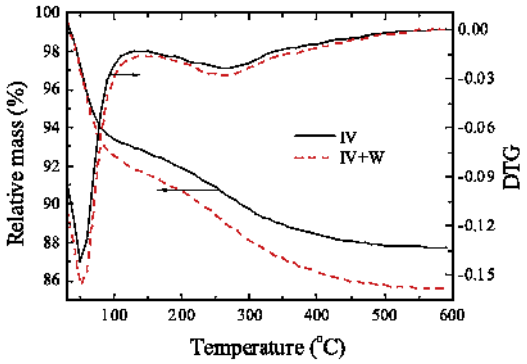


Figure6. Thermogravimetry curves of as-synthesized$TiO_2$ particles.

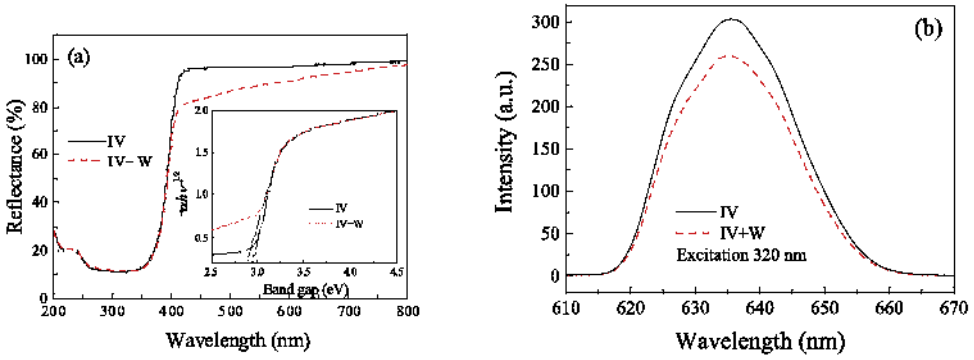


Figure 7. (a) Diffuse reflectance spectra and (b) photoluminescence (PL) spectra of as-synthesized $TiO_2$ particles.

### 3.5. Organic matter content analysis

The TGA curves of as-synthesized rutile-type $TiO_2$ particles are exhibited in figure 6. Comparing the TGA curves of both the IV and IV + W particles, we found that the thermal decomposition of both particles could be divided into two degradation stages. The first thermal degradation stage is located at below 100 °C, along with a sharp thermal decomposition temperature of 50.5 °C. This is because of the removal of surface absorbed and residual water absorbed by $TiO_2$ particles. The second thermal degradation stage occurs at around 266 °C combined with a small broad thermal decomposition peak from 140 °C to 330 °C. That is induced by the decomposition of organic compounds [61]. Furthermore, the residual weights are measured to be 87.76% and 85.64% for the IV and IV + W particles at the temperature of 600 °C, respectively. Thus, the relative mass of the hydrolysis components of wool keratin incorporated into the IV + W particles is estimated to be 2.12%.

.

### 3.6. Optical property analysis

The diffuse reflectance spectra of as-synthesized rutile-type $TiO_2$ particles are reported in figure 7(a). Both of as-synthesized rutile-type $TiO_2$ particles have the strong absorption of UV rays, and their spectra are almost overlapped in UV waveband. The average reflectances for both particles are larger than 81.5% under UV irradiation. In the visible light waveband, the average reflectance of the IV particle is estimated to be 96.77%, higher than 90.12% of the IV + W particle. It means that more visible light irradiation is absorbed by the organic compound derived from wool keratin in the IV + W particle. The co-doping of C, O, N, S, and Cl in the IV + W particle serves as a trapping center for electrons and holes, reducing the recombination rate of charge carriers [39]. The relationships between $(\alpha h\nu)^2$ and incident photon energy $(h\nu)$ for both particles are inserted in figure 7(a), where $\alpha$ is the absorption coefficient. The band gap of the IV + W particle is calculated to be 2.8 eV, which is smaller than 2.9 eV of the IV particle [58].

The PL spectra of as-synthesized rutile-type $TiO_2$ particles are shown in figure 7(b). It is confirmed that

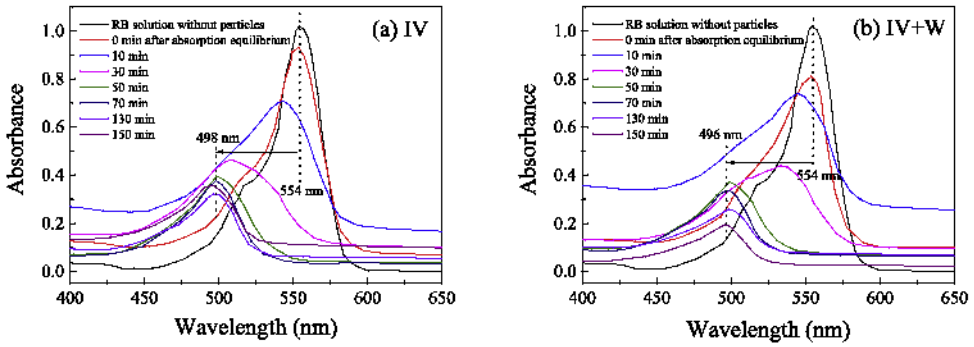


Figure 8. Absorbance curves of RB dye solution photodegraded by (a) IV and (b) IV + W$TiO_2$ particles under visible light irradiation.

the PL spectrum of $TiO_2$ is associated with its transfer behavior of photo-induced electrons and holes ($TiO_6$ octahedra and oxygen vacancies), reflecting the separation and recombination of charge carriers [62]. The broad emission bands are observed in the 620–660 nm range for both particles. However, the intensity of the IV + W particle is smaller than that of the IV particle, implying the higher charge-separation efficiency [63]. Thus, the low recombination rate of photogenerated electron-hole pairs for the IV + W particle results in the high photocatalytic activity.

### 3.7. Photocatalytic performance

The absorbance curves of RB dye solution photodegraded by the IV and IV + W $TiO_2$ particles at specific time intervals under visible light irradiation are compared in figure 8. After reaching the adsorption-desorption equilibrium, the absorbances of RB dye solutions at 554 nm decrease from 1.02 to 0.93 for the IV particle and 0.82 for the IV + W particle. It means that more RB dye molecules are adsorbed by the IV + W particle. The results of zeta potentials indicate that the zeta potential of the IV particle is -0.81, smaller than the zeta potential 6.31 of the IV + W particle. So the positively charged IV + W $TiO_2$ particle is liable to adsorb the cationic RB dye molecules. As the irradiation time increases, the absorbances of RB dye solution decrease gradually for both particles under visible light irradiation. This is ascribed to the destruction of the conjugated chromophore structure of RB [64]. At the same time, the characteristic absorption peaks at 554 nm are shifted to 498 nm for the IV particle and 496 nm for the IV + W particle, respectively. The hypsochromic shift is due to the formation of a series of N-deethylated intermediates of RB [64]. The decreased rate of absorbance for the IV + W particle is faster than that for the IV one. After 150 min of visible light irradiation, the corresponding absorbances are 0.32 at 498 nm and 0.19 at 496 nm for the IV and IV + W particles, respectively.

It is known that when rutile-type $TiO_2$ particles are irradiated by a ray equal or greater than the bandgap energy (3.0 eV), an electron is transferred from valence band to conduction band, which leads to a pair of holes and electrons on the surface of the $TiO_2$ particles. The photo-generated electrons reduce $Ti^{4+}$ cations to the $Ti^{3+}$ state and the holes oxidize $O^{2-}$ anions. During this process, the oxygen atoms are thrown out and a group of oxygen vacancies is produced on the surface. The water molecules in the solution can occupy the empty sites and the adsorbed OH groups are created on the surface, which increases the hydrophilicity of the $TiO_2$ surface. Meanwhile, the photo-generated electrons react with the oxygen molecules in the solution and produce superoxide radical anions ($O_2 \cdot -$). The photo-generated holes react with water and hydroxyl radicals ($\cdot OH$) are produced. These strong active species (hole, $\cdot OH$, and $O_2 \cdot -$) lead to the N-deethylation and the conjugated chromophore structure cleavage of RB dye [65], which finally results in the mineralization of the organic compounds caused by a series of radical chain reactions [66]. The rutile $TiO_2$ particles with high-energy exposed {001} and {101} facets have more atom steps, edges, kinks, and dangling bonds, which result in the high chemical activity [67]. The RB molecules adsorbed on the IV + W $TiO_2$ particle can absorb visible light to form dye radical cations in comparison with the IV one. The excited RB molecules can transfer the electron to the conduction band of $TiO_2$ and subsequently generate $O_2 \cdot -$ [68]. In addition, the photo-generated electrons and holes can be captured by the doping C, O, N, S, and Cl species and reduce the recombination of photogenerated electrons and holes [69].

The liquid environmental transmission electron microscopy and electron energy loss spectroscopy have revealed that a metastable hydrogenated shell containing reduced $Ti^{3+}$ ions can be produced on the surface of $TiO_2$ particles [70]. According to the XPS analysis, $Ti^{3+}$ ions on the surface of the IV particle have a band gap energy (2.9 eV) and thus are very reactive and play an important role in the photocatalytic process generated by using

visible light irradiation. The photocatalytic degradation of RB dye solution by the IV particle is attributed to the C–$T^{3+}$, O–$Ti^{3+}$, and Cl–$Ti^{3+}$ species. Importantly, the photocatalytic activity of the IV + W particle is significantly enhanced as compared with the IV particle. One reason is that less energy is required for an electron transition owing to the narrow energy band gap (2.8 eV) of $Ti^{3+}$ in rutile-type $TiO_2$ particle co-doped with C, O, N, S, and Cl elements, and this leads to the enhanced visible light absorption. The enhanced light absorption and oxidation power of $TiO_2$ co-doped with C, N, and Shave been proved by resonant x-ray emission spectroscopy measurements and localized density of states simulations, while the proton reduction capabilities are preserved [71]. Another reason is that the IV + W particle has a larger specific surface area and positive zeta potential.

## 4. Conclusions

In summary, we reported here the use of wool fibers on the modification of rutile-type $TiO_2$ photocatalyst based on the hydrothermal method. We compared the photocatalytic properties of the urchin-like rutile-type IV and IV + W $TiO_2$ particles for photodegradation of RB dye solution exposure to visible light irradiation. To investigate the differences in photoactivity between the above two particles, we identified the co-doping of carbon, oxygen, nitrogen, sulfur and chlorine, the larger specific surface area and the positive zeta potential affecting the photocatalytic activity of urchin-like rutile-type $TiO_2$ particles. We provided a simple scheme for incorporating of multiple elements into rutile-type $TiO_2$ particles by use of wools.

## Acknowledgements

This work was supported by the National Natural Science Foundation of China (No. 51873169) and the Sanqin Scholar Foundation (2017).

## References

[1] Ohno T, Sarukawa K and Matsumura M 2001 J. Phys. Chem. B 105 2417–20
[2] Andersson M, Osterlund L, Ljungstrom S and Palmqvist A 2002 J. Phys. Chem. B 106 12317–22
[3] Jung H S and Kim H 2009 Electron. Mater. Lett. 5 73–6
[4] ZhangJ F, Zhou P, Liu J J and Yu J G 2014 Phys. Chem. Chem. Phys. 16 20382–6
[5] Dong D B, Li P J, Li X J, Xu C B, Gong D W, Zhang Y Q, Zhao Q and Li P 2010 Chem. Eng. J. 158 378–83
[6] Kim S J, Lee J L, Lee E G, Lee H G, Kim S J and Lee K S 2003 J. Mater. Res. 18 729–32
[7] Li Y Z, Lee N H, Lee E G, Song J S and Kim S J 2004 Chem. Phys. Lett. 389124–8
[8] Yan J Q, Wu G J, Guan N J, Li L D, Li Z X and Cao X Z 2013 Phys. Chem. Chem. Phys. 1510978–88
[9] Yan T J, Yuan R S, Li W J and You J M 2014 Appl. Catal. A 478 204–10
[10] Kakuma Y, Nosaka A Y and Nosaka Y 2015 Phys. Chem. Chem. Phys. 1718691–8
[11] Yener H B, Yilmaz M, Deliismail O, Ozkan S F and Helvaci S S 2017 Sep. Purif. Technol. 173 17–26
[12] Li X B, Li T W, Wu C Z and Zhang Z D 2007 J. Nanopart. Res. 91081–6
[13] Zhao Z, Tan H Q, Zhao H F, Lv Y, Zhou L J, Song Y J and Sun Z C 2014 Chem. Commun. 50 2755–7
[14] Yurdakal S, Palmisano G, Loddo V, Augugliaro V and Palmisano L 2008 J. Am. Chem. Soc. 130 1568–9
[15] Masahashi N, Mizukoshi Y, Semboshi S and Ohtsu N 2009 Appl. Catal. B Environ. 90 255–61
[16] Bae E, Murakami N, Nakamura M and Ohno T 2010 Appl. Catal. A 380 48–54
[17] Lai L L and Wu JM 2015 Ceram. Int. 41 12317–22
[18] ZhangJ, Yan S, Fu L, Wang F, Yuan M Q, Luo G X, Xu Q, Wang X and Li C 2011 Chinese J. Catal. 32 983–91
[19] Cha S I, Hwang K H, Kim Y S, Yun M J, Seo S H, Shin Y J, Moon J H and Lee D Y 2013 Nanoscale 5 753–8
[20] Nowotny M K and Bahnemann D W 2011 Phys. Status Solidi RRL 5 92–4
[21] Hayashi K, Nakamura M, Makita Y, Fujiwara R, Kori T and Ishimura K 2011 Mater. Lett. 65 3037–40
[22] Sun B, Zhou G W, Zhang Y, Liu R R and Li T D 2015 Chem. Eng. J. 264125–33
[23] Wu T T, Kang X D, Kadi M W, Ismail I, Liu G and Cheng H M 2015 Chinese J. Catal. 36 2103–8
[24] Zhang J, Liu P L, Lu Z D, Xu G L, Wang X Y, Qian L S, Wang H B, Zhang E P, Xi J H and Ji Z G 2015J. Alloy. Compd. 632 133–9
[25] Yang Z W, Wang B, ZhangJ, Cui H, Pan Y, An H and Zhai J P 2015 Phys. Chem. Chem. Phys. 17 18670–6
[26] Pelaez M et al 2012 Appl. Catal. B Environ. 125 331–49
[27] Shieh D L, Lin Y S, Yeh J H, Chen S C, Lin B C and Lin J L 2012 Chem. Commun. 48 2528–30
[28] Ohno T, Tsubota T, Toyofuku M and Inaba R 2004 Catal. Lett. 98 255–8
[29] Sun H Q, Wang S B, Ang H M, Tade M O and Li Q 2010 Chem. Eng. J. 162 437–47
[30] Xiang G L, Wang Y G, Wu D, Li T Y, He J, Li J and Wang X 2012 Chem. Eur. J. 18 4759–65
[31] Wang J, Zhang G, Zhang Z H, Zhang X D, Zhao G, Wen F Y, Pan Z J, Li Y, Zhang P and Kang P L 2006 Water Res. 40 2143–50
[32] Jha P K, Gupta S K and Lukacevic I 2013 Solid State Sci. 22 8–15
[33] Belosevic-Cavor J, Batalovic K, Koteski V, Radakovic J and Rangel C M 2015 Int. J. Hydrogen Energ. 40 9696–703

[34] Duo F F, Wang Y W, Fan CM, Mao X M, Zhang X C, Wang Y F and Liu J X 2015 Mater. Charact. 99 8–16
[35] Devi L G, Nithya P M, Abraham C and Kavitha R 2017 Mater. Today Commun. 101–13
[36] Peng F C, Gao H L, Zhang G L, Zhu Z Q, ZhangJ and Liu Q J 2017 Materials 10 209 –1–14
[37] Fang W Z, Xing M Y and ZhangJ L 2017 J. Photochem. Photobiol. C-Photochem. Rev. 32 21–39
[38] Wu J, Lu H W, Zhang X L, Raziq F Z, Qu Q and Jing L Q 2016 Chem. Commun. 52 5027–9
[39] Wang F, Ma Z Z, Ban P P and Xu X H 2017 Mater. Lett. 195 143–6
[40] Erdogan N, Park J and Ozturk A 2016 Ceram. Int. 4216766–74
[41] Song X Y, Li W Q, He D, Wu H Y, Ke Z J, Jiang C Z, Wang G M and Xiao X H 2018 Adv. Energy Mater. 8 1800165 –1–8
[42] Popescu C and Hocker H 2007 Chem. Soc. Rev. 361282–91
[43] Zoccola M, Aluigi A, Patrucco A, Vineis C, Forlini F, Locatelli P, Sacchi M C and Tonin C 2012 Text. Res. J. 82 2006–18
[44] Wang Y W, Zhang L Z, Deng K J, Chen X Y and Zou Z G 2007 J. Phys. Chem. C 1112709–14
[45] de los Santos D M, Navas J, Aguilar T, Sanchez-Coronilla A, Alcantara R, Fernandez-Lorenzo C, Blanco G and Calleja J M 2015 Mater. Chem. Phys. 161 175–84
[46] He Z Q, Cai Q L, Fang H Y, Situ G H, Qiu J P, Song S and Chen J M 2013 J. Environ. Sci. (China) 25 2460–8
[47] Xu H, Zheng Z, Zhang L Z, Zhang H L and Deng F 2008 J. Solid State Chem. 181 2516–22
[48] Ohno T, Sarukawa K and Matsumura M 2002 New J. Chem. 261167–70
[49] Tian S, Yang H Q, Cui M, Shi R Y, Zhao H, Wang X W, Wang X Y and Zhang L Z 2011 Appl. Phys. A 104 149–58
[50] Akila Y, Muthukumarasamy N, Agilan S, Mallick T K, Senthilarasu S and Velauthapillai D 2016 Opt. Mater. 58 76–83
[51] Zhou X Y, Wang Z, Xia X H, Shao G S, Homewood K and Gao Y 2018 ACS Appl. Mater. Inter. (https://doi.org/10.1021/ acsami.8b07816)
[52] Zheng C Y, Li D, Wan J F, Yu X J and Xing Z P 2016 J. Nanosci. Nanotechnol. 1612573–81
[53] Groen J C, Peffer L A A and Perez-Ramirez J 2003 Micropor. Mesopor. Mat. 601–17
[54] Li S X, Chen J, Zheng F Y, Li Y C and Huang F Y 2013 Nanoscale 512150–5
[55] Groen J C and Perez-Ramirez J 2004 Appl. Catal. A 268121–5
[56] Zhang J, Fu W, Xi J H, He H, Zhao S C, Lu H W and Ji Z G 2013 J. Alloy. Compd. 575 40–7
[57] Ikuma Y, Ogoe S, Watanabe Y, Niwa K, Tajiri H and Sakata O 2013 J. Ceram. Soc. Jpn. 121 254–7
[58] Hu W B, Li L P, Tong W M, Li G S and Yan T J 2010 J. Mater. Chem. 20 8659–67
[59] Yang Y Q, Liu G, Irvine J T S and Cheng H M 2016 Adv. Mater. 28 5850–6
[60] Wang Z Q et al 2015J. Am. Chem. Soc. 137 9146–52
[61] Paola A D, Cufalo G, Addamo M, Bellardita M, Campostrini R, Ischia M, Ceccato R and Palmisano L 2008 Colloid. Surface. A 317 366–76
[62] Lei Y, Zhang L D, Meng G W, Li G H, Zhang X Y, Liang C H, Chen W and Wang S X 2001 Appl. Phys. Lett. 781125–7
[63] Kroeze J E, Savenije T J, Vermeulen M J W and Warman J M 2003 Phys. Chem. B 107 7696–705
[64] Hu X F, Mohamood T, Ma W H, Chen C C and Zhao J C 2006 J. Phys. Chem. B 110 26012–8
[65] Wang P, Cheng M M and Zhang Z H 2014 J. Saudi Chem. Soc. 18 308–16
[66] Carp O, Huisman C L and Reller A 2004 Prog. Solid State Ch. 32 33–177
[67] Cai D, Yang T, Liu B, Wang D, Liu Y, Wang L, Li Q and Wang T A 2014 J. Mater. Chem. A 213990–5
[68] Zheng X Z, Li D Z, Li X F, Yu L H, Wang P, Zhang X Y, Fang J L, Shao Y and Zheng Y 2014 Phys. Chem. Chem. Phys. 1615299–306
[69] Zhao Z, Zhang X Y, Zhang G Q, Liu Z Y, Qu D, Miao X, Feng P Y and Sun Z C 2015 Nano Res. 8 4061–71
[70] Lu Y, Yin W J, Peng K L, Wang K, Hu Q, Selloni A, Chen F R, Liu L M and Sui M L 2018 Nat. Commun. 9 2752 –1–9
[71] Sa J, Garlisi C, Palmisano G, Czapla-Masztafiak J, Kayser Y and Szlachetko J 2018 Mater. Chem. Phys. 208 281–8